Revision 3

Experimental study of the formation of chalcopyrite and bornite via the sulfidation of hematite: mineral replacements with a large volume increase.

Jing Zhao[1,2] Joël Brugger[1,] , Guorong Chen[3], Yung Ngothai[2] and Allan Pring[1,4*]

[1]Department of Mineralogy, South Australian Museum, North Terrace, Adelaide, SA 5000, Australia

[2]School of Chemical Engineering, University of Adelaide, Adelaide, SA 5005, Australia

[3] Key Laboratory for Ultrafine Materials of Ministry of Education, School of Materials Science and Engineering, East China University of Science and Technology, Shanghai 200237, China

[4]School of Chemistry and Physics, University of Adelaide, Adelaide, SA 5005, Australia

*Corresponding author: allan.pring@samuseum.sa.gov.au

Abstract

Chalcopyrite ($CuFeS_2$) and bornite (Cu_5FeS_4) are the most abundant Cu-bearing minerals in hydrothermal Cu deposits, forming under a wide range of conditions from moderate temperature sedimentary exhalative deposits to high temperature porphyry Cu and skarn deposits. We report the hydrothermal synthesis of both chalcopyrite and bornite at 200-300 °C under hydrothermal conditions. Both minerals formed via the sulfidation of hematite in solutions containing Cu(I) (as a chloride complex) and hydrosulfide, at pH near the pK_a of H_2S(aq) over the whole temperature range. Polycrystalline chalcopyrite formed first, followed by bornite.

Assuming that Fe behaves conservatively, the transformation of hematite to chalcopyrite involves a large increase in volume (~290%). The reaction proceeds both via direct replacement of the existing hematite and via overgrowth around the grain. Chemical exchanges between bulk solution and hematite are enabled by a network of μm-size pores. However, in some cases the chalcopyrite overgrowth develops large grain sizes with few apparent pores and in these cases fluid transport may have been via a network of fractures. Similarly to the replacement of hematite by chalcopyrite, bornite forms via the replacement of chalcopyrite. The reaction has a large positive volume (~230%), and proceeds both via chalcopyrite replacement and via overgrowth.

This study shows that replacement reactions can proceed via coupled dissolution-reprecipitation even where there is a large volume increase between parent and product mineral. This study also provides further evidence about the controls of reaction pathways onto the final mineral assemblage. In this case, the host initial fluid was under saturated with respect to Fe-bearing minerals. Upon slow release of Fe at the surface of hematite, a mineral assemblage of chalcocite, bornite, and finally chalcopyrite is expected. However, in practice chalcocite did not nucleate on the surface of hematite. Rather relatively slow nucleation of bornite enabled high concentrations of Fe to build up near the dissolving hematite, so that chalcopyrite (high sulfidation experiments) or chalcopyrite+pyrite (low sulfidation) crystallized first.

Keywords: hematite, chalcopyrite, bornite, mineral replacement, hydrothermal experiment.

Introduction

Chalcopyrite and bornite are the most abundant Cu-bearing sulfides and are the primary Cu minerals in a wide range of ore deposits from moderate temperature sedimentary exhalative (SEDEX) deposits, through Fe oxide Cu gold (IOCG) deposits, to high temperature porphyry Cu deposits and skarns (Robb 2005). Whatever the ore deposit type, chalcopyrite and bornite are essentially hydrothermal minerals, formed from Cu-rich saline hydrothermal fluids. Much of our knowledge of the phase relations in the Cu-Fe-S system is based on experimental studies undertaken using the classic dry sealed tube technique, which serve to inform our understanding of subsolidus processes, but may not provide an accurate view of controls on mineral formation under hydrothermal conditions (see Fleet 2006, Vaughan and Craig 1978).

There have been very few experimental studies on chalcopyrite or bornite formation under hydrothermal conditions relevant for ore formation. Barnard and Christopher (1966 a,b) recrystallized crushed chalcopyrite grains in pure water and in Cl-rich solutions at temperatures between 400 and 500 °C, and observed that chalcopyrite recrystallized in Cl-rich solutions but not in pure water. This result is consistent with the poor stability of the Cu(I) aqua ion in aqueous solutions (disproportionation to Cu(II) and Cu(0)), and the importance of Cl-complexing for the transport of Cu(I) in hydrothermal solutions (Brugger et al. 2007; Etschmann et al. 2010). Kojima and Sugaki (1985) studied the phase relations in the Cu-Fe-Zn-S system between 300 and 500 °C under hydrothermal conditions by the recrystallization of chalcopyrite, bornite, and other sulfides in a 5 *m* NH_4Cl solution. These authors did not report the direct synthesis of chalcopyrite or bornite hydrothermally. Seyfried and Ding (1993) conducted a series of experiments to investigate the effects of redox, temperature and fluid chemistry on the solubility of Cu- and Fe-bearing sulfide minerals in Na-K-Cl aqueous fluids in relation to sub-seafloor hydrothermal systems. But again, they used chalcopyrite as a starting material rather than studying its formation. Hu et al. (1999) synthesized chalcopyrite nanoparticles by dissolving CuCl(s), $FeCl_3 \cdot 6H_2O$(s), and $(NH_4)_2S$(s) in aqueous solutions in autoclaves at 200-250 °C for 3 hrs. The resulting chalcopyrite took the form of nanorods typically 20-40 nm in diameter and up to several μm in length. Wang et al.

(2009) used a similar method but let the reaction run for 24 hrs to make chalcopyrite nanowires of slightly wider diameter and greater length. Neither of these direct synthesis methods yielded euhedral chalcopyrite typical of that found in nature.

Recently we have used dissolution-reprecipitation reactions to synthesize, and study the formation of, a range of important sulfide ore minerals including pyrite (Qian et al. 2010, 2013), violarite (Tenailleau et al. 2006, Xia et al. 2008, 2009a, Brugger et al. 2010), and marcasite (Qian et al. 2011). Chalcopyrite is principally a hydrothermal mineral, and forms in some cases in open cavities (veins), and in other cases as a replacement of preexisting minerals. The replacement of hematite by chalcopyrite has been reported from a number of different ore-forming environments, including Kupferschiefer type deposits (Kucha and Pawlikowski 1986) and IOCG deposits (Kiruna type; Edfelt et al. 2005). We undertook to study the formation of chalcopyrite by the replacement of hematite and magnetite under hydrothermal conditions up to 300 °C under vapor-saturated pressures.

Samples and methods

Hematite and magnetite sources

Natural micaceous hematite (SA Museum sample G6983) from Cumberland, England was used throughout this study. To investigate the effects of the form and nature of the Fe oxide source on the transformation, needle-shape kidney ore hematite (SA Museum sample G1603) from Cumberland, England and natural magnetite crystals from the Mt. Isa area, Queensland (SA Museum sample G8146) were used in addition to micaceous hematite. The identification of the minerals was confirmed by powder X-ray diffraction and their chemical purity was determined by electron probe microanalysis (EMP) using a Cameca SX-51 instrument (20 kV, 20 nA) at Adelaide Microscopy, University of Adelaide. The following standards were used: Fe (Fe_2O_3) and (Fe_3O_4); Si, Al and Mg ($Mg_3Al_2(SiO_4)_3$); P ($Ca_5(PO_4)_3F$; Mn ($MnSiO_3$) and V (V metal). Details of the compositions of the parent minerals are given in the Table 1. Crystals were washed in an ultrasonic bath, ground, and sieved into a 125 to 150 μm size fraction.

Preparation of solutions and chemicals

Buffer solutions (including acetate, phosphate, and borate) ranging from $pH_{25°C}$ 3-11 were used as background solutions throughout this study at 1 m or 0.2 m concentrations (the solution compositions are listed in the Table 2). The buffer solutions were prepared using boiled high purity water (conductivity of 18 MΩ cm^{-1}; Direct - Q3 system, Millipore corp.) in an argon-filled anoxic glove box at room temperature (~ 25 °C), which aims to remove the dissolved O_2 and CO_2. Sodium chloride (1 molal; m) was added into each solution to prevent Cu (I) from devolving into Cu (II) and Cu (0) (Brugger et al. 2007). The pH values of solutions at room temperature were measured before experiments. The pH values at reaction temperatures (Table 3) were calculated using the HCh geochemical modeling software (Shvarov and Bastrakov 1999), assuming full dissociation of thioacetamide into H_2S. All chemical reagents used in the experiments were analytical grade, including copper(I) chloride which was provided by Hopkin and Williams Ltd. and thioacetamide supplied by Scharlau Chemie SA. Copper (I) chloride was purified before experiments using the procedure of Keller and Wycoff (1946) to remove any Cu(II) impurities. Thioacetamide was used as a source of H_2S. Thioacetamide is added as a poorly soluble solid at room temperature, and it breaks down above 100 °C, liberating H_2S (Qian et al. 2011):

$$CH_3CSNH_2 + H_2O \rightarrow CH_3CONH_2 + H_2S_{(aq)} \quad (1)$$

Hydrothermal experiments

Experiments were undertaken under both low and high S conditions (S_{tot} = 0.05 and 0.5 molal, respectively). During the reaction, the pH in the high S conditions was buffered by $H_2S(aq)/HS^-$. Small amounts of acetate, phosphate and borate anions (0.2 m) were added to better constrain the pH, by controlling the $H_2S(aq)/HS^-$ ratio. The different buffers used also enabled the monitoring of the reproducibility and of the potential effects of the buffer components on the reaction progress. To study the effect of pH on the reaction, low S experiments were conducted using 1 m buffer solutions ranging from $pH_{25\,°C}$ 4-10.

For all runs, the solids (Fe oxide, CuCl(s) and thioacetamide) were accurately weighed into titanium autoclaves with an 8 mL internal volume. Then 5 mL of background buffer solution was added into the autoclave within an argon-filed anoxic glove box. The sealed autoclaves were removed from the glove box and placed in pre-heated electric furnaces (at temperature up to 300 ˚C; temperature regulation precision of ± 2 °C) for the required reaction time (up to 360 hrs). At the end of experiments, the autoclaves were quenched to room temperature in a large volume of cold water (~10 L). The reacted fluid was collected and the pH value of solution was measured after reaction. Solids were rinsed three times with Milli-Q water and then three times with acetone before drying. Results from leaking runs were not used. During the experiments, the pressures in the autoclaves are autogenous (~86 bar at 300 °C).

To explore the effect of temperature on the reaction mechanism and the kinetics, a series of experimental high S runs (0.5 m S) were carried out at temperatures of 200-300 ˚C, using 0.2 m buffer solutions as background solutions. Reaction time ranged from 20 to 360 hrs and the ratio between the weight of micaceous hematite and the background solution volume was fixed at 1.25 g/L. For each run, 10 mg of micaceous hematite (SAM G6983), 12.5 mg CuCl(s), and 189 mg thioacetamide were loaded into the autoclaves. In these experiments the pH is buffered primarily by S. The $pH_{25°C}$ values measured, after quenching, were 5.50, 5.60 and 5.96 for background solutions A5, P7, and B10, respectively.

The needle hematite experiments were run at 250 °C for 140 hrs, using 0.2 m background solutions P3 and A5. The amount of hematite, CuCl, and thioacetamide were 10 mg, 12.5 mg and 189 mg, respectively. In addition, magnetite experiments were run at 300 °C for 140 hrs, using 0.2 m background solutions A5, P7, B10 and P11. The amount of magnetite, CuCl, and thioacetamide were 10, 12.8, and 194 mg, respectively.

For the series of low sulfidation experiments, the amount of S was reduced by an order of magnitude (18.9 mg thioacetamide; ~0.05 m S), and a more concentrated buffer (1 m) solution was used. Hence, the pH during these experiments was controlled by the buffer, rather than by S. The low sulfidation experiments were conducted at 300 °C for 90 hrs in

a number of different buffer solutions, to allow direct comparison of the nature of the products and reaction extents as a function of pH.

Analysis methodology

The identification of the minerals and quantitative phase analysis was undertaken using room-temperature powder X-ray diffraction (XRD) patterns collected using a Huber Guinier Image Plate G670 with $CoK_{\alpha 1}$ radiation (λ= 1.78892 Å). Diffraction data in the 2θ range from 20 to 80° was collected. The extent of the transformation was determined by Rietveld quantitative phase analysis (QPA) of powder X-ray diffraction data (Rietveld 1969) using the program Topas (Bruker AXS 2009). A Pseudo-Voigt function and 6^{th} order Chebychev polynomial were used to model the peak shapes and the background, respectively. The zero shift and scale factors (S) were refined. Crystal structural data of minerals for QPA and EBSD were taken from the ICSD database (hematite #82902; chalcopyrite #94554; bornite #24174; magnetite #31157; pyrite #15012; pyrrhotite #9146).

Characterization of the morphological and textural features of reacted was undertaken using a Philips XL30 field emission scanning electron microscope (FESEM) at Adelaide Microscopy, University of Adelaide. The composition of products from selected experiments was determined by electron probe microanalysis in WDS mode using a Cameca SX-51 instrument at Adelaide Microscopy, University of Adelaide, operated at an accelerating voltage of 20 kV and a beam current of 20 nA. The following standard was used: Cu Fe and S ($CuFeS_2$). Electron backscatter diffraction (EBSD) analyses were performed using an EDAX-TSL EBSD system fitted to a FEI Helios NanoLab DualBeam FIB/SEM platform at Adelaide Microscopy.

Results

Conditions of chalcopyrite and bornite formation

We conducted experiments at two different sulfidation levels. To investigate the effect of pH on the reaction products, a series of experiments were conducted at 300 °Cunder low

sulfidation conditions (0.05 m H_2S) in background solutions consisting of 1 m acetate or borate buffers, and 1 m NaCl (Table 3). These low S experiments (runs L1-L7; Table 3) show that hematite was replaced by chalcopyrite under acidic to slightly basic conditions ($pH_{300°C}$ 4.59 to 6.06); small amounts of Fe sulfides (pyrite or pyrrhotite) were also formed under these conditions. In contrast, hematite transformed to magnetite under basic conditions ($pH_{300°C}$ 7.50 to 9.16). For example, around 54% (weight percentage) of hematite was replaced by chalcopyrite (26%) and pyrite (28%) at $pH_{300°C}$ 4.59 after 90 hrs reaction (Run No. L1), while hematite was totally replaced by magnetite at $pH_{300°C}$ 9.16 under similar conditions (L7). Bornite was observed only in the run at $pH_{300°C}$ 6.06.

The high sulfidation experiments contained an equivalent of 0.5 m H_2S. In those experiments, high concentrations of buffer would be required to fix pH beyond the $H_2S(aq)/HS^-$ buffer. Hence, all reactions at high sulfidation were conducted near the $pK_a(H_2S(aq))$. The background solutions contained 1 m NaCl as well as ~0.2 m of different buffer solutions, aimed at defining the $H_2S(aq)/HS^-$ ratio and testing the effect of background solution on the reaction. Over the course of the reactions, the solutions changed from clear to a black suspension (thought to be Cu_2S**)** resulting from the reaction of Cu(I) with the $H_2S_{(aq)}$, and then cleared as the reaction proceeded. For example, the solution from experiment B27 (300 °C for 20 hrs; Table 3) was a dark suspension, while those at the same temperature after 140 hrs (B29) or longer were clear with only a few H_2S bubbles.

For the high sulfidation experiments, XRD analyses confirms that hematite has been replaced by chalcopyrite and bornite under hydrothermal conditions over the temperature range of 200 to 300 °C. No reaction was observed after 360 hrs at 150 ˚C. The proportion of the products shows a first order dependence on the reaction conditions. For example, after 140 hrs reaction in background solution A5 at 250 °C (Run No. B15), around 40% (weight percentage) of hematite has been replaced by chalcopyrite (29%) and bornite (11%). As the temperature increased to 275 °C (B26), the extent of transformation increased to 61%, including 37% of chalcopyrite and 24% of bornite.

The precipitation of bornite was only observed at temperatures > 200 °C when more than 35% of the hematite had been converted to chalcopyrite. At 200 °C, no bornite was

observed even when 27% of the hematite had been replaced by chalcopyrite (B3). The percentages of bornite are normally less than 30%, depending on the total reaction time. In some cases, we also observed a decrease in the amount of bornite over the duration of the reaction. For example, experiments undertaken in background solution A5 at 300 °C for 20 to 360 hrs (B27-B31) show that the percentage of bornite increases from 16% to 27% over the first 50 hrs of the reaction, and then decreases to zero for the 360 hrs run. The proportions of product phases are shown as pie charts in Figure 1.

Products and textures

After reaction, the grain size increased significantly compared to that of the hematite. The micaceous hematite flakes were replaced by golden yellow grains of chalcopyrite and sometimes admixed with a small number of purple grey grains of bornite. The micaceous hematite gains are characterized by sharp-edges and smooth surface before reactions. After 140 h reaction at 300 °C, the product particles were considerably enlarged with round edges (Fig. 2a). The surface of the golden yellow grains was covered by tetrahedral crystals of chalcopyrite reaching sizes up to 2 μm across (Fig. 2b). The average compositions of chalcopyrite (24 points) and bornite (17 points) are $Cu_{1.03(3)}Fe_{1.04(5)}S_{1.93(5)}$ and $Cu_{5.24(9)}Fe_{0.92(8)}S_{3.84(7),}$ respectively (Table 4). The bornite composition at $Bn_{90}Dg_{10}$ falls on the bornite-dignetite solid solution join. Although many bornites in nature have a near-stoichiometric composition (Cu_5FeS_4), Cu-rich compositions such as that in our experiments are only reported from a few deposits, such as the granite-associated Cu-Ag-(Au)-Mo veins at Moberg, Telemark, Norway (Cook et al. 2011).

Back-scattered electron images of cross sections of grains show that the replacement process initiates at the outer surface of the original hematite grains and along cracks within the grains (Fig. 2c). Small gaps (< 1 μm) and cracks commonly appear at the reaction interface between chalcopyrite and hematite. Figure 2d shows two hematite grains that were wrapped together by the chalcopyrite layer resulting in an enlarged grain. Layering defined by differences in the size and density of pores is commonly observed within the chalcopyrite. For example chalcopyrite in the grain shown in Figure 2c contains only a few fine visible pores in the inner part adjacent to the hematite core,

while in the outer zone, corresponding to an overgrowth, the pores are more numerous and on a scale of 1 to 2 μm. The EBSD analyses show that the chalcopyrite rim is polycrystalline (Fig. 3). No crystallographic relationship between the chalcopyrite and the hematite substrate could be established.

In contrast to chalcopyrite, the surface of the bornite grains is quite rough (Fig. 4a), showing a complex growth of pyramidal and stepped cube faces (Fig. 4b). The cross-section images of many bornite grains (e.g., Fig. 4c) reveal three layers: an outer layer of bornite (light grey), a middle layer of chalcopyrite (grey), and hematite at the core (dark grey). The reaction interfaces between chalcopyrite and hematite and between chalcopyrite and bornite can be sharp, but locally display a higher density of pores and cracks (Figs. 4c-e). Both the chalcopyrite and bornite are porous with the pore size in bornite the coarser of the two. Bornite rims usually contain an inner porous zone and an outer zone with few pores (e.g., Fig. 4e). This outer zone shows evidence of idiomorphic bornite crystals growing into the solution. Figure 4f shows a section through a grain that has been mostly (possibly completely) replaced by bornite. The bornite displays an inner zone with high porosity and a porosity-free outer zone. The grain is also cut by a conjugate set of fractures.

Effect of the nature of the Fe source

Experiments with needle-shaped crystals of hematite (G1603) rather than flakes (G6983) were run at 250 °C for 140 hrs in background solutions P3 and A5. X-ray diffraction patterns confirm that kidney ore hematite has been replaced by chalcopyrite and bornite under all studied conditions. Similar amounts of chalcopyrite (8% and 10%, respectively) replaced kidney hematite in background solutions P3 and A5 at 250 °C and over 140 hrs (K1-K2), while about 40% of micaceous hematite were replaced by chalcopyrite (29%) and bornite (11%) under the same reaction conditions (details shown in Table 5).

Magnetite was replaced by chalcopyrite and bornite in background solutions A5, P7, B10 and P11 at 300 °C and over a 140 h reaction time (M1-M4). The XRD pattern of the parent magnetite (Appendix, Fig. A2b) shows that the starting mineral contains 19 wt% hematite. After reaction, only magnetite, chalcopyrite and bornite appear, indicating that

hematite is preferentially replaced by the Cu Fe sulfide minerals (Fig. 5b). The reaction extent (Table 5) for runs in background solutions A5, P7, B10 and P11 were 61%, 64%, 69% and 62%, respectively. These results can be compared to experiments using micaceous hematite under the same conditions (64% for B29; 67% for B32; 72% for B33 and 74% for B35, respectively) and show that the extent of reaction are equivalent in different background solutions given the statistical uncertainties with QPA.

Effect of background solution

Experimental runs exploring the effects of background solution on the transformation of hematite to chalcopyrite were undertaken by measuring the extent of reaction under fixed conditions (T = 250 °C, $[Cl^-]$ = 1 m) for solutions P3, A5, P7 and B10 (Table 3). The transformation occurs in all solutions used, and the plots of extent of reaction versus time show a consistent trend (Fig. 1a). BSE images and EDS analyses of samples from experiments using the phosphate buffer revealed a layer of Cu-Fe phosphate at the reaction front between hematite and chalcopyrite (Fig. 5). The amounts of Cu-Fe phosphate were, however, too small to be detected by powder XRD.

Effect of reaction temperature

Experiments conducted at different temperatures but under otherwise similar conditions show that higher temperatures favor the replacement reaction. For example, as shown in Figure 1b, the extent reaction for solution A5 (runs B3, B9, B16, and B31) increases from 27% to 83% as the temperature increases from 200 to 300 ˚C. Utilizing solution B10, the extent of runs B4, B10, B22, and B34 increases from 20% at 200 °Cto 74% at 300 ˚C. It is important to note that the hydrolysis rate of thioacetamide to form $H_2S(aq)/HS^-$ was effectively constant over this temperature range (Qian et al. 2010), so that the above results truly reflect the effect of temperature on the replacement reaction rate.

Experiments performed from 20-360 hrs at temperatures ranging from 200 to 300 °C using solution A5 further confirm that higher temperatures favor the replacement reaction. The reaction kinetic at different temperatures can be modeled using the Avrami equation:

$$\ln\{\ln[1/(1-y)]\} = n\ln(k) + n\ln(t) \quad (2)$$

where y is the reaction extent (disappearance of hematite or magnetite), t (s) is the reaction time, k (s^{-1}) is the rate constant, and n (dimensionless) is a time exponent depending on the reaction mechanism (Avrami 1939, 1940, 1941; Christian 1965). If the activation energy does not change during the reaction, a plot of $\ln\{\ln[1/(1-y)]\}$ vs. $\ln(t)$ yields a straight line from which the exponent n and the rate constant k can be determined (e.g., Wang et al. 2005a,b; Zhao et al. 2009). The results of experiments, conducted at different temperatures, are shown by the linear behavior on plots of $\ln\{\ln[1/(1-y)]\}$ vs. $\ln(t)$ (Fig. 6). The calculated time exponents n and rate constants k for the temperature series are summarized in Table 6. Note that there is no noticeable change in the texture of the products with temperature, and the values of the time exponent n are all within error (95% confidence level; average $n = 0.31(2)$).

Discussion

Reaction mechanism for the replacement of hematite by chalcopyrite

The replacement of hematite by chalcopyrite under the hydrothermal conditions utilized in this study is a fluid-meditated process. Reaction textures in the form of a reaction front progressing along grain rims and along fractures within the grains; reaction interfaces varying from sharp with no visible gap to areas with gaps several μm wide; e.g., Figs. 2c, 2d and 4d); and the sensitivity of the product to fluid parameters such as pH (low S experiments) are consistent with a dissolution-reprecipitation reaction mechanism (Putnis 2009; Xia et al. 2009a,b).

The overall reaction of hematite transformation to chalcopyrite can be written as:

$$Fe_2O_3(hm) + 2CuCl_2^- + 4H_2S(aq) = 2CuFeS_2(cpy) + 4Cl^- + 2H^+ + 3H_2O \quad (3)$$

In dissolution-reprecipitation reactions, the kinetics of reaction and the reaction textures are controlled by the interplay between the dissolution and precipitation reactions. The dissolution of hematite results in aqueous Fe complexes entering the solutions. Fe(II) is the most stable form of Fe in hydrothermal solutions (Fein et al. 1992; Testemale et al. 2009). Speciation calculations indicate that Fe solubility is low under our experimental conditions, due to the high S content (~1 ppb, as Fe^{2+}, $FeCl^+$, $FeCl_2(aq)$, and $Fe(OH)^+$

complexes). These calculations assume that redox is controlled by S and that the equilibrium Fe(III) solubility (< 1 ppt) is controlled by $Fe(OH)_3(aq)$ and $Fe(OH)_4^-$ complexes. Reductive dissolution of hematite is an efficient process even at room temperature (Panias et al. 1996). Therefore it is likely that some Fe in solution in our experiment is reduced to Fe(II), resulting in the oxidation of some of the S. The reductive dissolution of hematite in our experiments can be written:

$$Fe_2O_3(hm) + 6H^+ + 2e^- = 2Fe^{2+} + 3H_2O. \quad (4)$$

Reaction (3) is coupled with the oxidation of S, e.g.,

$$¼\,[H_2S(aq) + 4H_2O = SO_4^{2-} + 10H^+ + 8e^-]. \quad (5)$$

Note that reaction (5) is unlikely to represent the real process since intermediary S oxidation states, likely catalyzed at the mineral surfaces, may dominate the Fe reduction pathway. The dissolution rate depends (Lasaga 1998) on (i) the temperature; (ii) the activities of aqueous species acting as inhibiting or catalyzing agents, most prominently Fe^{2+} (Panias et al. 1996); (iii) the reactive surface area of the hematite (Echigo et al. 2012); and (iv) the undersaturation level of hematite (Hersman et al. 1995). The linear behavior of the Avrami plots (Fig. 6) indicates that the reaction rate is limited by the solubility of hematite through a porous product and that the reactions are not fluid transport limited. It is possible to calculate an activation energy from the above kinetic data using the Arrhenius equation, but this figure would not represent the Ea of chalcopyrite formation but is rather related to the hematite dissolution.

The precipitation of chalcopyrite can be described by the reaction:

$$Cu(HS)_2^- + Fe^{2+} + 2H_2S(aq) = CuFeS_2 + 2H^+ + e^-. \quad (6)$$

Reaction (6) is an oxidation reaction. The replacement of hematite by chalcopyrite may involve redox reactions even if this is not apparent in the overall reaction (3). In solutions where sulfide is the predominant S species, it is expected that Cu(I) will be the dominant oxidation state for Cu, in the form of hydrosulfide or chloride complexes (Brugger et al. 2007; Estchmann et al. 2010; Liu et al. 2001, 2005; Mountain and Seward 1999, 2003; Xiao et al., 1998). Speciation calculations show that CuHS(aq) and $Cu(HS)_2^-$ are the predominant Cu complexes in the high S solutions at reaction

365 temperatures. According to equation (6), the rate of chalcopyrite precipitation may be
366 affected by the concentration and speciation of the aqueous Cu, Fe, and S species. Since
367 abundant Cu and S sources are present in solution, the concentration of Fe^{2+} complexes
368 (controlled by the dissolution rate of hematite) is likely to exert a first order control on
369 the rate of chalcopyrite precipitation.

370 The precipitation of chalcopyrite consumes Fe from the solution at the reaction front and
371 further enhances the dissolution rate of hematite by releasing H^+ (eq. 6). Thus the
372 hematite dissolution and the chalcopyrite precipitation processes drive each other (eq. 4),
373 and the supersaturation state of chalcopyrite in the fluid is maintained at the reaction front
374 by continuous dissolution and reprecipitation. This process should continue until all the
375 hematite is consumed. However for every volume dissolved, ~2.9 times greater volume
376 of chalcopyrite precipitates. This is clearly not possible at the reaction front. The fact
377 that the reaction can progress to completion is related to the ability of the excess Fe to
378 travel (most likely as a Fe(II) complex) to the outside of the grain, where it contributes to
379 an overgrowth of chalcopyrite.

380 ## *Reaction end-points: the roles of nucleation and growth*

381 The precipitation of chalcopyrite and bornite can be divided into two parts: (1) nucleation
382 and (2) crystal growth. Bornite has not been noted to form at the reaction interface
383 between hematite and chalcopyrite, but only on the outer surface of some of the
384 chalcopyrite grains. Usually, only a small number of grains in each reaction batch
385 contained bornite, the majority consisting of chalcopyrite over hematite. During the
386 transformation of hematite to chalcopyrite, the chalcopyrite can further react with Cu and
387 S in the solution to form bornite. The overall reaction for the formation of bornite from
388 chalcopyrite can be written:

389 $$CuFeS_2(s) + 4CuCl(aq) + 2H_2S(aq) \rightarrow Cu_5FeS_4(s) + 4HCl(aq) \quad (7)$$

390 The importance of nucleation is illustrated by Figure 7, which shows that our
391 experimental solutions were initially saturated with respect to chalcocite. Cu-sulfides
392 indeed nucleate in solution (possibly mostly during quenching), but no evidence for

nucleation of Cu-sulfides on the surface of hematite was found. The dissolution of hematite progressively increases the concentration of Fe(II) aqueous species at the reaction front. With increasing concentration of Fe in the Cu-S bearing solution, bornite solubility is reached first (Fig. 7). Yet, the first phase to precipitate is chalcopyrite rather than bornite or chalcocite. This suggests that nucleation of both chalcocite and bornite at the reaction front is much more difficult than chalcopyrite, enabling the building up of Fe concentrations near the dissolving surface. Faster nucleation of chalcopyrite relative to bornite (even at lower saturation level) results in chalcopyrite usually forming first. As soon as a thin chalcopyrite rim forms, crystal growth rather than nucleation controls the system, and new chalcopyrite can be added to the substrate from both the hematite and solutions sides. This dissolution-reprecipitation process continues until all of the hematite has dissolved and most of the chalcopyrite has precipitated.

Replacement reactions with large volume increases

Pseudomorphic reactions proceed via *interface* coupled dissolution re-precipitation mechanisms, where the dissolution of the parent phase is coupled to the precipitation of the product phase at the reaction front (see Putnis 2009). The volume change associated with dissolution and precipitation reactions during mineral replacement is a critical factor for the advancement of the reaction. Contrary to solid-state reactions, the overall volume change of a replacement reaction is controlled not only by the molar volume of parent and product, but also by their solubility ratio within a given solution (Pollok et al. 2011). Because components can be provided by, or removed via the solution, coupled dissolution-reprecipitation reactions can show a large increase or decrease in molar volumes between parent and product. Pseudomorphic replacement via *interface* coupled dissolution-reprecipitation reactions have been previously observed for reactions with nominal volume changes varying from 0.21 to 1.6 (in Table 7).

The transformation reaction of hematite to chalcopyrite and bornite both have extremely large volume increases. Based on Fe conservation, the transformation of hematite into chalcopyrite is accompanied by a volume increase on the order of 290%, and the transformation of chalcopyrite to bornite by a volume increase of 226%. Such a large volume increase precludes pseudomorphic replacement except in the initial stages of the

reaction. The reactions in this study are similar to the reaction of magnetite dissolution and pyrite precipitation, which results in a volume increase of 65%, and proceeds via both replacement and overgrowth (Qian et al. 2010).

Chalcopyrite was not observed to nucleate and grow on the sides of the autoclaves, which is consistent with the fact that nucleation of chalcopyrite is difficult. For the replacement reaction to commence the dissolution of a small amount of hematite at the reaction front results in a fluid boundary layer that is supersaturated with respect to the chalcopyrite. This leads to heterogeneous nucleation (possibly catalyzed by the hematite surface) and subsequent growth of chalcopyrite from this solution layer. For the reaction to proceed following nucleation, solution transport from the hematite-chalcopyrite interface and the bulk solution must continue, as must the dissolution of hematite, since hematite is the only source of Fe in the system. Initially the chalcopyrite will nucleate and grow near the site of hematite dissolution, but as the reaction proceeds the large volume expansion produces increasing strain at the interface. This stress at the hematite surface propagates cracks in the hematite, which in turn facilitates nucleation and growth of chalcopyrite within these cracks (e.g., Fig. 2c). The volume increase associated with the precipitation of chalcopyrite forces the cracks apart enabling further chalcopyrite growth (e.g., Jamtveit et al. 2009). The chalcopyrite rims are overgrown with small chalcopyrite crystals consistent with growth from the bulk solution onto the outside of the grains. This overgrowth is less compact and more porous than the chalcopyrite growing at the hematite contact. The chalcopyrite overgrowth can cause the cementing of distinct hematite grains (Fig. 2d). In contrast, bornite overgrowth can take the form of blocky bornite crystals. In this case exchanges between the bulk fluid and the reaction fronts (chalcopyrite/bornite; hematite/chalcopyrite) occur via a set of factures through the bornite (Fig. 4f).

Geological implications

In this study, we demonstrate that chalcopyrite and bornite can form under mild hydrothermal conditions from Cu- and S-bearing solutions interacting with Fe oxides (hematite, magnetite). Although direct replacement of hematite by Cu-Fe sulfides is relatively rarely observed, fluid-rock interaction is an important process that can release Fe in solution and contribute to the

formation of Fe-Cu sulfides. The replacement of hematite offers microscopic insight into this process. Because of the large volume increase associated with this replacement (nearly a factor of 3), most of the sulfide precipitation occurs as overgrowths on the outside of the grains. In this situation, both chalcopyrite and bornite form idiomorphic crystals. The nature of the sulfides in the experiments is controlled by the reaction conditions affecting the relative nucleation of chalcopyrite and bornite. Similar processes are likely to play important roles in nature since the scale of Fe transport can vary from μm (as in the experiments) to meters in nature, with sulfides forming both via replacement and in structurally controlled open spaces such as veins.

Acknowledgement

We thank Len Green, Aoife McFadden, and Benjamin Wade from Adelaide Microscopy Center for their assistance in using the FESEM, EBSD, ICP-MS, and electron microprobe. The constructive comments of David Vaughan, an anonymous referee and associate editor Daniel Harlov greatly improved the clarity of the text of this paper. This work has been made possible by the financial support of the Australian Research Council (Grant DP1095069).

Reference

Avrami, M. (1939) Kinetics of phase change I. Journal of Chemical Physics, 7, 1103-1112.

Avrami, M. (1940) Kinetics of phase change II. Journal of Chemical Physics, 8, 212-224.

Avrami, M. (1941) Granulation, phase change and microstructure. Journal of Chemical Physics, 9, 177-184.

Barnard, W.M. and Christopher, P.A. (1966a) Hydrothermal synthesis of chalcopyrite. Economic Geology, 61, 897-902.

Barnard, W.M. and Christopher, P.A. (1966b) Further study on the effectiveness of aqueous solutions in the hydrothermal synthesis of chalcopyrite. Economic Geology, 61, 1287-1290.

Brugger, J., Etschmann, B., Liu, W., Testemale, D., Hazemann, J.L., Emerich, H., van Beek, W., and Proux, O. (2007) An XAS study of the structure and thermodynamics of Cu(I) chloride complexes in brines up to high temperature (400 °C, 600 bar). Geochimica et Cosmochimica Acta, 71(20), 4920-4941.

Brugger, J., McFadden, A., Lenehan, C.E., Etschmann, B., Xia, F., Zhao, J., and Pring, A. (2010) A Novel Route for the Synthesis of Mesoporous and Low-Thermal Stability Materials by Coupled Dissolution-Reprecipitation Reactions: Mimicking Hydrothermal Mineral Formation. CHIMIA International Journal for Chemistry, 64, 693-698.

Bruker AXS (2009): TOPAS V4.2: General profile and structure analysis software for powder diffraction data. Bruker AXS GmbH, Karlsruhe, Germany.

Christian, J.W. (1965) The theory of transformations in metals and alloys, 975p. Pergamon Press, Oxford.

Cook, N.J., Ciobanu, C.L., Danyushevsky, L.V., and Gilbert, S. (2011) Minor and trace elements in bornite and associated Cu-(Fe)-sulfides: A LA-ICP-MS study. Geochimica Cosmochima Acta, 75(21), 6473-6496.

Echigo, T., Aruguete, D.M., Murayama, M., and Hochella, M.F. (2012) Influence of size, morphology, surface structure, and aggregation state on reductive dissolution of hematite nanoparticles with ascorbic acid. Geochimica et Cosmochimica Acta, 90, 149-162.

Edfelt, Å., Armstrong, R., Smith, M., and Martinsson, O. (2005) Alteration paragenesis and mineral chemistry of the Tjårrojåkka apatite–iron and Cu (-Au) occurrences, Kiruna area, northern Sweden. Mineralium Deposita, 40, 409-434.

Etschmann, B.E., Liu, W., Testemale, D., Muller, H., Rae, N.A., Proux, O., Hazemann, J.L., and Brugger, J. (2010) An in situ XAS study of copper(I) transport as hydrosulfide complexes in hydrothermal solutions (25-592 ˚C, 180-600 bar): Speciation and solubility in vapor and liquid phases. Geochimica et Cosmochimica Acta, 74(16), 4723-4739.

508 Fein, J.B., Hemley, J.J., D'Angelo, W.M., Komninou, A., and Sverjensky, D.A. (1992)
509 Experimental study of iron-chloride complexing in hydrothermal fluids.
510 Geochimica et Cosmochimica Acta, 56, 3179-3190.

511 Fernández-Díaz, L., Pina, C.M., Astilleros, J.M., and Sánchez-Pastor, N. (2009) The
512 carbonatation of gypsum: Pathways and pseudomorph formation. American
513 Mineralogist, 94, 1223-1234.

514 Fleet, M.E. (2006) Phase Equilibria at High Temperatures. Reviews in Mineralogy and
515 Geochemistry, 61(1), 365-419.

516 Hersman, L., Lloyd, T., and Sposito, G. (1995) Siderophore-promoted dissolution of
517 hematite. Geochimica et Cosmochimica Acta, 59(16), 3327-3330.

518 Hu, J., Lu, Q., Deng, B., Tang, K., Qian, Y., Li, Y., Zhou, G., and Liu, X. (1999) A
519 hydrothermal reaction to synthesize $CuFeS_2$ nanorods. Inorganic Chemistry
520 Communications, 2(12), 569-571.

521 Jamtveit, B., Putnis, C., and Malthe-Sorenssen, A. (2009) Reaction induced fracturing
522 during replacement processes. Contributions to Mineralogy and Petrology, 157,
523 127-133.

524 Kasioptas, A., Perdikouri, C., Putnis, C.V., and Putnis, A. (2008) Pseudomorphic
525 replacement of single calcium carbonate crystals by polycrystalline apatite.
526 Mineralogical Magazine, 72(1), 77-80.

527 Keller, R.N. and Wycoff, H.D. (1946) Copper (I) chloride. Inorganic Syntheses, 2, 1-4.

528 Kojima, S. and Sugaki, A. (1985) Phase relations in the Cu-Fe-Zn-S system between
529 500 °C and 300 °C under hydrothermal conditions. Economic Geology, 80(1),
530 158-171.

531 Kucha, H. and Pawlikowski, M. (1986) Two-brine model of the genesis of strata-bound
532 Zechstein deposits (Kupferschiefer type), Poland. Mineralium Deposita, 21(1),
533 70-80.

534 Lasaga, A.C. (1998) Kinetic Theory in the Earth Sciences. Princeton University Press,
535 New Jersey.

536 Liu, W., McPhail, D.C., and Brugger, J. (2001) An Experimental Study of Copper(I)-
537 Chloride and Copper(I)-Acetate Complexing in Hydrothermal Solutions between
538 50°C and 250°C and Vapor-Saturated Pressure. Geochimica et Cosmochimica
539 Acta, 65(17), 2937-2948.

540 Liu, W. and McPhail, D.C. (2005) Thermodynamic properties of copper chloride
541 complexes and copper transport in magmatic-hydrothermal solutions. Chemical
542 Geology, 221(1-2), 21-39.

543 Mountain, B.W. and Seward, T.M. (1999) The hydrosulphide/sulphide complexes of
544 copper(I): experimental determination of stoichiometry and stability at 22°C and
545 reassessment of high temperature data. Geochimica et Cosmochimica Acta, 63(1),
546 11-29.

547 Mountain, B.W. and Seward, T.M. (2003) Hydrosulfide/sulfide complexes of copper(I):
548 Experimental confirmation of the stoichiometry and stability of $Cu(HS)_2^-$ to
549 elevated temperatures. Geochimica et Cosmochimica Acta, 67(16), 3005-3014.

550 Panias, D., Taxiarchou, M., Douni, I., Paspaliaris, I., and Kontopoulos, A. (1996)
551 Dissolution of hematite in acidic oxalate solutions: the effect of ferrous ions
552 addition. Hydrometallurgy, 43, 219-230.

553 Pollok, K., Putnis, C.V., and Putnis, A. (2011) Mineral replacement reactions in solid
554 solution-aqueous solution systems: volume changes, reactions paths and end-
555 points using the example of model salt systems. American Journal of Science, 311,
556 211-236.

557 Putnis, C.V., Geisler, T., Schmid-Beurmann, P., Stephan, T., and Giampaolo, C. (2007)
558 An experimental study of the replacement of leucite by analcime. American
559 Mineralogist, 92, 19-26.

560 Putnis, A. (2009) Mineral Replacement Reactions. Reviews in Mineralogy and
561 Geochemistry, 70(1), 87-124.

562 Qian, G., Brugger, J., Skinner, W.M., Chen, G., and Pring, A. (2010) An experimental
563 study of the mechanism of the replacement of magnetite by pyrite up to 300 °C.
564 Geochimica et Cosmochimica Acta, 74(19), 5610-5630.

Qian, G., Xia, F., Brugger, J., Skinner, W.M., Bei, J., Chen, G., and Pring, A. (2011) Replacement of pyrrhotite by pyrite and marcasite under hydrothermal conditions up to 220 °C: An experimental study of reaction textures and mechanisms. American Mineralogist, 96(11-12), 1878-1893.

Qian, G., Brugger, J., Testemale, D., Skinner, W., and Pring, A. (2013) Formation of As(II)-pyrite during experimental replacement of magnetite under hydrothermal conditions. Geochimica et Cosmochimica Acta, 100, 1-10.

Rietveld, H. (1969) A profile refinement method for nuclear and magnetic structures. Journal of Applied Crystallography, 2(2), 65-71.

Robb, L. (2005) Introduction to ore-forming processes. Blackwell Publishing, Oxford.

Seyfried Jr., W.E. and Ding, K. (1993) The effect of redox on the relative solubilities of copper and iron in Cl-bearing aqueous fluids at elevated temperatures and pressures: An experimental study with application to subseafloor hydrothermal systems. Geochimica et Cosmochimica Acta, 57(9), 1905-1917.

Shvarov, Y., and Bastrakov, E. (1999) HCh: a software package for geochemical modelling. User's guide. AGSO record, 1999/25, 60p.

Tenailleau, C., Pring, A., Etschmann, B., Brugger, J., Grguric, B., and Putnis, A. (2006) Transformation of pentlandite to violarite under mild hydrothermal conditions. American Mineralogist, 91, 706-709.

Testemale, D., Brugger, J., Liu, W.H., Etschmann, B., and Hazemann, J.L. (2009) In-situ X-ray absorption study of Iron(II) speciation in brines up to supercritical conditions. Chemical Geology, 264(1-4), 295-310.

Vaughan, D.J. and Craig, J.R. (1978) Mineral chemistry of metal sulphides. Cambridge University Press, Cambridge.

Wang, H., Pring, A., Ngothai, Y., and O'Neill, B. (2005a) A low-temperature kinetic study of the exsolution of pentlandite from the monosulfide solid solution using a refined Avrami method. Geochimica et Cosmochimica Acta, 69, 415-425.

592 Wang, H., Pring, A., Xia, Y., Ngothai, Y., and O'Neill, B. (2005b) Phase evolution and
593 kinetics of the oxidation of monosulfide solid solution under isothermal
594 conditions. Thermochimica Acta, 427, 13-25.

595 Wang, M.X., Wang, L.S., Yue, G.H., Wang, X., Yan, P.X., and Peng, D.L. (2009) Single
596 crystal of $CuFeS_2$ nanowires synthesized through solventothermal process.
597 Materials Chemistry and Physics, 115(1), 147-150.

598 Xia, F., Zhou, J., Brugger, J., Ngothai, Y., O'Neill, B., Chen, G., and Pring, A. (2008).
599 Novel Route To Synthesize Complex Metal Sulfides: Hydrothermal Coupled
600 Dissolution-Reprecipitation Replacement Reactions. Chemistry of Materials 20(8),
601 2809-2817.

602 Xia, F., Brugger, J., Chen, G., Ngothai, Y., O'Neill, B., Putnis, A., and Pring, A. (2009a)
603 Mechanism and kinetics of pseudomorphic mineral replacement reactions: A case
604 study of the replacement of pentlandite by violarite. Geochimica et
605 Cosmochimica Acta, 73(7), 1945-1969.

606 Xia, F., Brugger, J., Ngothai, Y., O'Neill, B., Chen, G., and Pring, A. (2009b). Three-
607 Dimensional Ordered Arrays of Zeolite Nanocrystals with Uniform Size and
608 Orientation by a Pseudomorphic Coupled Dissolution-Reprecipitation
609 Replacement Route. Crystal Growth & Design 9(11), 4902-4906.

610 Xiao, Z., Gammons, C.H., and Williams-Jones, A.E. (1998) Experimental study of
611 copper(I) chloride complexing in hydrothermal solutions at 40 to 300°C and
612 saturated water vapor pressure. Geochimica et Cosmochimica Acta, 62(17), 2949-
613 2964.

614 Zhao, J., Brugger, J., Grundler, P.V., Xia, F., Chen, G., and Pring, A. (2009) Mechanism
615 and kinetics of a mineral transformation under hydrothermal conditions:
616 Calaverite to metallic gold. American Mineralogist, 94(11-12), 1541-1555.

617 Zhao, J., Brugger, J., Xia, F., Ngothai, Y , Chen, G., and Pring, A. (2013) Dissolution-
618 reprecipitation versus solid-state diffusion: mechanism of mineral transformations
619 in sylvanite, $(AuAg)_2Te_4$, under hydrothermal conditions. American Mineralogist,
620 98(1), 19-32.

621

622

623

624

Figure Captions

Figure 1. Reaction extent as a function of (a) time and (b) temperature. For (a), all experiments were conducted at 250 °C for different fluid compositions. Experiments were operated for up to 360 hrs. For (b), experiments were conducted in background solution A5 and B10 at temperatures over 200 to 300 ˚C, and at a fixed reaction time of 360 hrs. Errors of the reaction extent (3σ; ±5%) are plotted at each point. Pie charts above and below the plots show the proportions of phases after reaction for the A5 and B10 series, respectively. In the chart, hematite is presented in black, chalcopyrite in light grey, and bornite in dark grey.

Figure 2. Secondary electron images showing reaction textures from hydrothermal reactions forming chalcopyrite. (a) Round edges of a reacted grain, showing the preservation of the external dimensions of the primary hematite grains (Run No. B3). (b) Surface of a chalcopyrite-bearing grain showing fine tetrahedral crystals varying in size up to 2 μm across (B25). Backscattered electron image of the cross section of a partially reacted grain. (c) Cross-section through a partially reacted grain, showing that the reaction develops along grain surfaces and cracks (B30). The inset shows the detail of the porosity changes in the chalcopyrite near the surface of the grain. (d) Two hematite grains fused together by the overgrowth of the chalcopyrite layer (B28).

Figure 3. EBSD analyses of hematite and chalcopyrite along phase boundaries of one grain from sample B31. (a-b) {001} pole figures presenting the orientation and distribution of hematite and chalcopyrite in the corresponding regions. (c) Crystal orientations of hematite (left in green) and chalcopyrite (right in multi colors) along the phase boundaries. Each color in this figure relates to one crystal orientation. Hematite is single crystal and chalcopyrite is polycrystalline with more than 4 orientations (in the colors of purple, yellow, green and blue).

Figure 4. Secondary electron (a,b) and back scatted electron images(c-f) showing the textures of bornite. (a) Grain covered with bornite overgrowth (Run No.B29) showing a rough morphology. (b) Detail view of the surface of a bornite grain shown in (a). (c) Cross section of three layered grain, which include a bornite layer (light grey), a chalcopyrite layer (grey) and a hematite layer (dark grey) from the outside to the core (B29). (d) Sharp boundaries between hematite, chalcopyrite and bornite (B16). (e) Channels at the boundaries between hematite and chalcopyrite. (f) Cross section of a bornite grain with porous core and fractured, low porosity rim (B33).

Figure 5. Secondary electron image (SEM) and element distribution maps of Na, P, Fe, Cu, and S for a partially replaced grain in Run No. B32, showing high concentrations of P and Na at the reaction front between hematite and chalcopyrite.

Figure 6. Kinetics of the replacement of hematite by chalcopyrite at different temperatures. Plots showing the linear regression according to Equation 2 for runs at different temperatures. Time (t) is in seconds. Error bars correspond to a 5% point error (3 σ) on the reaction extent. Results from the linear regressions are given in Table 6. Pie

charts at the bottom illustrate the percentages of hematite, chalcopyrite and bornite in reactions operated in background solution A5 at 300 °C (B27-B31), and illustrate the formation and transformation of bornite.

Figure 7. Activity-activity diagram illustrating the mineral stability fields and reaction paths in the experiments at 250 ˚C, high sulphidation (a) and at 300 ˚C, low sulphidation (b). The initial solution is Fe-free, and supersaturated with respect to chalcocite. In (a), the grey arrow shows the paragenetic sequence for a solution saturated with Cu and S coupled with the slow addition of Fe by dissolution of hematite via chalcocite → bornite → chalcopyrite. Instead, the experiments showed precipitation of chalcopyrite first, followed by bornite. In (b), the results of runs buffered at different pHs illustrate the complexity of the controls on the experimental products. White numbers are buffer pHs; black circles indicate possible equilibrium assemblages (the presence of pyrrhotite depends upon the redox state of the fluid), grey circles indicate non-equilibrium assemblage.

Tables

Table 1. Composition of starting materials

Hematite (G6983) (21 points) (wt%)				Kidney ore hematite (G1603) (18 points) (wt%)				Magnetite (G8146) (13 points) (wt%)			
	M	**R**	**S**		**M**	**R**	**S**		**M**	**R**	**S**
Fe_2O_3	97.33	94.35-100.69	0.36	Fe_2O_3	96.92	95.06-98.66	0.36	Fe_3O_4	99.25	99.67-100.52	0.38
SiO_2	1.21	<0.06-2.98	0.06	SiO_2	1.21	0.96-1.35	0.06	VO_2	0.61	0.58-0.65	0.03
Al_2O_3	0.05	<0.06-0.17	0.06	Al_2O_3	0.04	<0.02-0.11	0.02	SiO_2	0.03	<0.03-0.04	0.03
MgO	0.04	<0.05-0.10	0.05	MnO_2	0.03	<0.02-0.06	0.02	Al_2O_3	0.03	<0.03-0.07	0.03
MnO_2	0.03	<0.06-0.08	0.06	P_2O_5	0.06	<0.05-0.11	0.05	MgO	0.02	<0.02-0.03	0.02
P_2O_5	0.04	<0.05-0.13	0.05	CaO	≤0.06		0.06	MnO	0.05	<0.03-0.09	0.03
Total	98.53			Total	98.32			Total	99.99		

Note: "M" stands for mean, "R" for range and "S" for standard deviation.
* XRD analysis of the natural magnetite gave 81 ± 5 wt% magnetite and 19 ± 5 wt% hematite.

Table 2. Composition of buffer solutions

Buffer ID	$pH_{25°C}$		Components					
	calc.	**meas**	**Acid**	**C/m**	**Basic**	**C/m**	**Addition**	**C/m**
P3	3.10	2.98	H_3PO_4	0.0170	$NaH_2PO_4{\cdot}2H_2O$	0.1820	NaCl	1
A5	5.06	4.88	CH_3COOH	0.0590	CH_3COONa	0.1400	NaCl	1
P7	7.03	6.90	$NaH_2PO_4{\cdot}2H_2O$	0.0680	Na_2HPO_4	0.1310	NaCl	1
B10	10.1	9.80	H_3BO_3	0.1064	NaOH	0.0936	NaCl	1
P11	10.8	10.8	Na_2HPO_4	0.2000	NaOH	0.0282	NaCl	1
CA4	3.99	3.86	CH_3COOH	0.826	CH_3COONa	0.174	NaCl	1
CA5	5.06	4.88	CH_3COOH	0.296	CH_3COONa	0.704	NaCl	1
CA6	5.92	5.73	CH_3COOH	0.549	CH_3COONa	0.955	NaCl	1
CP7	7.03	6.90	$NaH_2PO_4{\cdot}2H_2O$	0.340	Na_2HPO_4	0.655	NaCl	1
CP8	8.08	8.02	$NaH_2PO_4{\cdot}2H_2O$	0.045	Na_2HPO_4	0.954	NaCl	1
CB9	9.10	8.76	H_3BO_3	0.704	NaOH	0.295	NaCl	1
CB10	10.1	9.80	H_3BO_3	0.532	NaOH	0.480	NaCl	1

701
702 Table 3. Reaction conditions and results
703

No.	Run No.	T/(°C)	Buffer Solution[†]	pH_T[‡]	Time (h)	NaCl /m	Products and molar percentage (wt%)[§]
L1	H300D4PH90HS	300	CA4	4.59	90	1	Hm(46)Cpy(26)Py(28)
L2	H300D5PH90HS	300	CA5	5.38	90	1	Hm(27)Cpy(38)Py(15)Po(19)
L3	H300D6PH90HS	300	CA6	6.06	90	1	Hm(78)Mgt(14)Cpy(4)Bn(4)
L4	H300D7PH90HS	300	CP7	7.50	90	1	Hm(96) Mgt(4)
L5	H300D8PH90HS	300	CP8	8.16	90	1	Hm(90) Mgt(10)
L6	H300D9PH90HS	300	CB9	8.56	90	1	Hm(81) Mgt(19)
L7	H300D10PH90HS	300	CB10	9.16	90	1	Mgt(100)
B1	H200D5PH50HS	200	A5	5.28	50	1	Hm(81)Cpy(19)
B2	H200D5PH140HS	200	A5	5.28	140	1	Hm(79)Cpy(21)
B3	H200D5PH360HS	200	A5	5.28	360	1	Hm(73)Cpy(27)
B4	H200D10PH360HS	200	B10	6.31	360	1	Hm(80)Cpy(20)
B5	H225D3PH360HS	225	P3	5.23	360	1	Hm(51)Cpy(36)Bn(13)
B6	H225D5PH20HS	225	A5	5.27	20	1	Hm(86)Cpy(14)
B7	H225D5PH50HS	225	A5	5.27	50	1	Hm(75)Cpy(25)
B8	H225D5PH140HS	225	A5	5.27	140	1	Hm(67)Cpy(33)
B9	H225D5PH360HS	225	A5	5.27	360	1	Hm(62)Cpy(32)Bn(6)
B10	H225D10PH360HS	225	B10	6.22	360	1	Hm(60)Cpy(31)Bn(9)
B11	H250D3PH20HS	250	P3	5.10	20	1	Hm(92)Cpy(8)
B12	H250D3PH50HS	250	P3	5.10	50	1	Hm(80)Cpy(20)
B13	H250D3PH140HS	250	P3	5.10	140	1	Hm(62)Cpy(27)Bn(11)
B14	H250D5PH50HS	250	A5	5.25	50	1	Hm(90)Cpy(10)
B15	H250D5PH140HS	250	A5	5.25	140	1	Hm(60)Cpy(29)Bn(11)
B16	H250D5PH360HS	250	A5	5.25	360	1	Hm(45)Cpy(45)Bn(10)
B17	H250D7PH20HS	250	P7	5.44	20	1	Hm(89)Cpy(11)
B18	H250D7PH90HS	250	P7	5.44	90	1	Hm(68)Cpy(20)Bn(12)
B19	H250D7PH140HS	250	P7	5.44	140	1	Hm(56)Cpy(31)Bn(13)
B20	H250D10PH20HS	250	B10	6.16	20	1	Hm(89)Cpy(11)
B21	H250D10PH90HS	250	B10	6.16	90	1	Hm(68)Cpy(24)Bn(9)
B22	H250D10PH360HS	250	B10	6.16	360	1	Hm(45)Cpy(28)Bn(27)
B23	H275D5PH20HS	275	A5	5.23	20	1	Hm(64)Cpy(25)Bn(11)
B24	H275D5PH50HS	275	A5	5.23	50	1	Hm(45)Cpy(41)Bn(14)
B25	H275D5PH90HS	275	A5	5.23	90	1	Hm(58)Cpy(24)Bn(18)
B26	H275D5PH140HS	275	A5	5.23	140	1	Hm(39)Cpy(37)Bn(24)
B27	H300D5PH20HS	300	A5	5.23	20	1	Hm(51)Cpy(33)Bn(16)
B28	H300D5PH50HS	300	A5	5.23	50	1	Hm(41)Cpy(32)Bn(27)
B29	H300D5PH140HS	300	A5	5.23	140	1	Hm(36)Cpy(44)Bn(20)
B30	H300D5PH240HS	300	A5	5.23	240	1	Hm(32)Cpy(55)Bn(12)
B31	H300D5PH360HS	300	A5	5.23	360	1	Hm(18)Cpy(83)
B32	H300D7PH140HS	300	P7	6.49	140	1	Hm(33)Cpy(55)Bn(11)
B33	H300D10PH140HS	300	B10	6.38	140	1	Hm(28)Cpy(52)Bn(21)
B34	H300D10PH360HS	300	B10	6.38	360	1	Hm(26)Cpy(62)Bn(12)
B35	H300D11PH140HS	300	P11	6.71	140	1	Hm(26)Cpy(56)Bn(18)
B36	C300D5PH140HS	300	A5	4.88	140	1	Cpy(49)Bn(51)
B37	C300D7PH140HS	300	P7	6.90	140	1	Cpy(43)Bn(57)
B38	C300D10PH140HS	300	B10	6.38	140	1	Cpy(50)Bn(50)
B39	12H250D3PH90HS	250	P3	5.10	90	1	Hm(71)Cpy(21)Bn(8)
B40	23H250D3PH90HS	250	P3	5.10	90	1	Hm(88)Cpy(9)Bn(3)
B41	DH250D3PH90HS	250	P3	5.10	90	1	Hm(93)Cpy(7)

B42	TH250D3PH90HS	250	P3	5.10	90	1	Hm(90)Cpy(9)Bn(1)

† "P" phosphate buffer solution, "A" acetate buffer solution, and "B" borate buffer solution. For respective compositions refer to Table 2.
‡ pH values were calculated at reaction temperature using the HCh software.
§ Obtained from powder X-ray diffraction patterns by Rietveld quantitative phase analysis. "Hm" stands for hematite, "Cpy" for chalcopyrite phase, "Bn" for bornite, "Py" for pyrite, "Pyt" for pyrrhotite, and "Mgt" for magnetite. Error on the phase proportion is estimated to 5% on each determination.

Table 4. Composition of products

Chalcopyrite (24 points) (wt%) Average composition of $Cu_{1.03(3)}Fe_{1.04(5)}S_{1.93(5)}$				**Bornite (17 points) (wt%)** Average composition of $Cu_{5.24(9)}Fe_{0.92(8)}S_{3.84(7)}$			
	M	**R**	**S**		**M**	**R**	**S**
Cu	65.60	63.48-67.22	1.94	Cu	35.34	32.22-35.50	0.99
Fe	10.10	9.57-11.31	0.24	Fe	31.49	30.00-32.39	0.70
S	24.30	22.92-24.91	0.68	S	33.44	32.22-35.50	0.98
Total	100.00			Total	100.27		

Note: "M" stands for mean, "R" for range, and "S" for standard deviation.

Table 5. Summary of effects on the nature iron sources

Reaction Solution	Kidney hematite (250°C) No.	Products and molar percentage (wt%)	Micaceous hematite (250°C) No.	Products and molar percentage (wt%)
P3	K1	Hm(92)Cpy(8)	B13	Hm(62)Cpy(27)Bn(11)
A5	K2	Hm(90)Cpy(10)	B15	Hm(60)Cpy(29)Bn(11)

Reaction Solution	Magnetite (300°C) No.	Products and molar percentage (wt%)	Micaceous hematite (300°C) No.	Products and molar percentage (wt%)
A5	M1	Mgt(39)Cpy(38)Bn(23)	B29	Hm(36)Cpy(44)Bn(20)
P7	M2	Mgt(36)Cpy(43)Bn(21)	B32	Hm(33)Cpy(55)Bn(11)
B10	M3	Mgt(31)Cpy(49)Bn(20)	B33	Hm(28)Cpy(52)Bn(21)
P11	M4	Mgt(38)Cpy(38)Bn(24)	B35	Hm(26)Cpy(56)Bn(18)

Table 6. Calculated time exponent n and rate constant k using Avrami Equation, as a function of temperature T.

T (°C)	pH_T	Background solution	n*	ln(k) [ln(s^{-1})]*	R^2
200	5.28	A5	0.28 ± 0.08	-17.8 ± 1.1	0.838
225	5.27	A5	0.29 ± 0.02	-16.3 ± 0.2	0.992
250	5.28	A5	0.40 ± 0.04	-14.7 ± 0.5	0.985
275	5.22	A5	0.30 ± 0.04	-14.0 ± 0.5	0.958
300	5.23	A5	0.31 ± 0.06	-12.7 ± 0.8	0.897

Note: Values for n and k correspond to the linear regressions shown in Figures 7a–7f.
*Standard deviations on k were calculated using the errors on n (the slope) and the error on the intercept using following equation:

$$\mathbf{S_k} = \sqrt{\mathbf{S_n^2} + \mathbf{S_I^2}}$$

733 Table 7. Nominal volume changes and textures during some dissolution-reprecipitation
734 reactions
735

Reaction	Conservative ion	Volume change (product over parent)	Replacement texture
Hematite→chalcopyrite	Fe	2.89	replacement and overgrowth (this study)
Chalcopyrite→bornite	Fe	2.26	replacement and overgrowth (this study)
Magnetite→pyrite	Fe	1.60	replacement and overgrowth (Qian et al. 2010)
Leucite→analcime	Al-Si	1.29	Pseudomorphic; large porosity of the product despite volume increase (Putnis et al. 2007, Xia et al. 2009b)
Pyrrhotite→pyrite	Fe	1.16	Pseudomorphic with minor overgrowth (Qian et al. 2011)
Sylvanite→calaverite	Au	0.96	Pseudomorphic (Zhao et al. 2013)
Calcite→hydroxyapatite	Ca	0.86	Pseudomorphic (Kasioptas et al. 2008)
Pentlandite→violarite	S	0.83	Pseudomorphic (Tenailleau et al. 2006, Xia et al. 2009a)
Calcite→fluorite	Ca	0.78	Pseudomorphic with a porous reaction rim (Putnis 2009)
Pyrrhotite→ pyrite/marcasite	S	0.69/0.71	Pseudomorphic (Qian et al. 2011)
Gypsum→calcite	Ca	0.50	Pseudomorphic (Fernández-Díaz et al. 2009)
Calaverite→gold	Au	0.21	Pseudomorphic (Zhao et al. 2009)

Note: All mineral data used in the calculation is from http://webmineral.com/data/

736
737

(a)

Reaction Extent / %

0
10
20
30
40
50
60

0
50
100
150
200
250
300
350
400

Reaction Time / h

P3
A5
P7
B10

(b)

Reaction Extent / %

10
20
30
40
50
60
70
80
90
100

200
220
240
260
280
300

T / °C

pH10
pH5

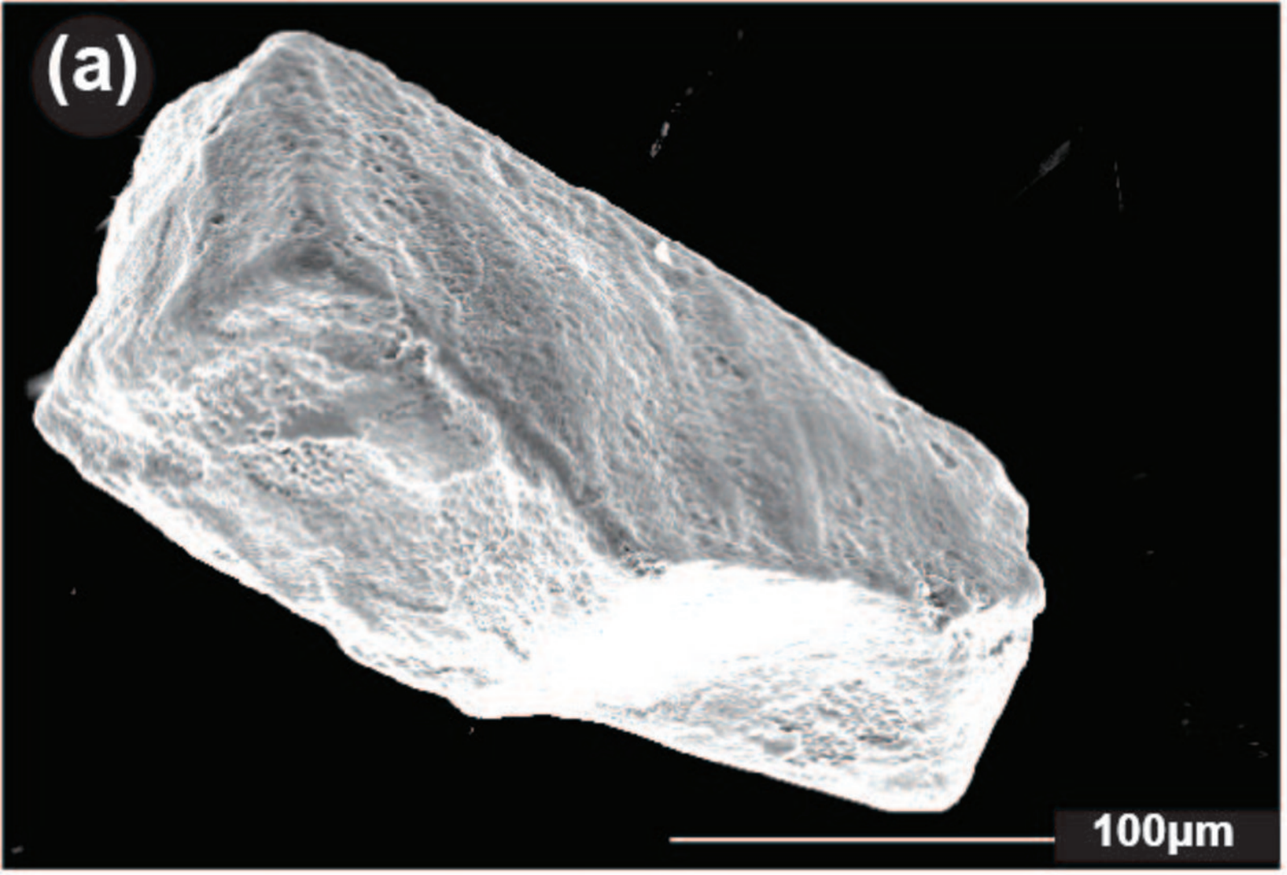
(a)
100μm

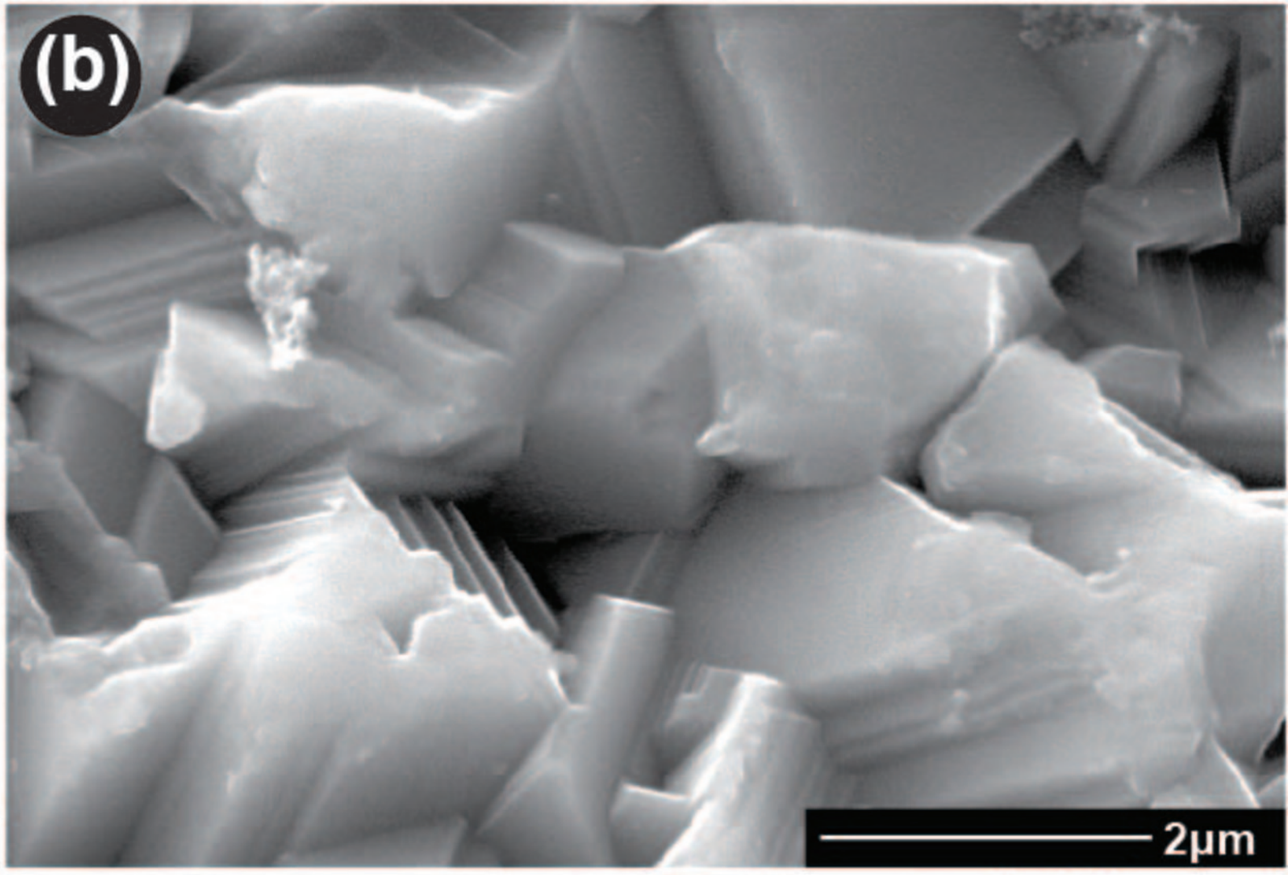
(b)
2μm

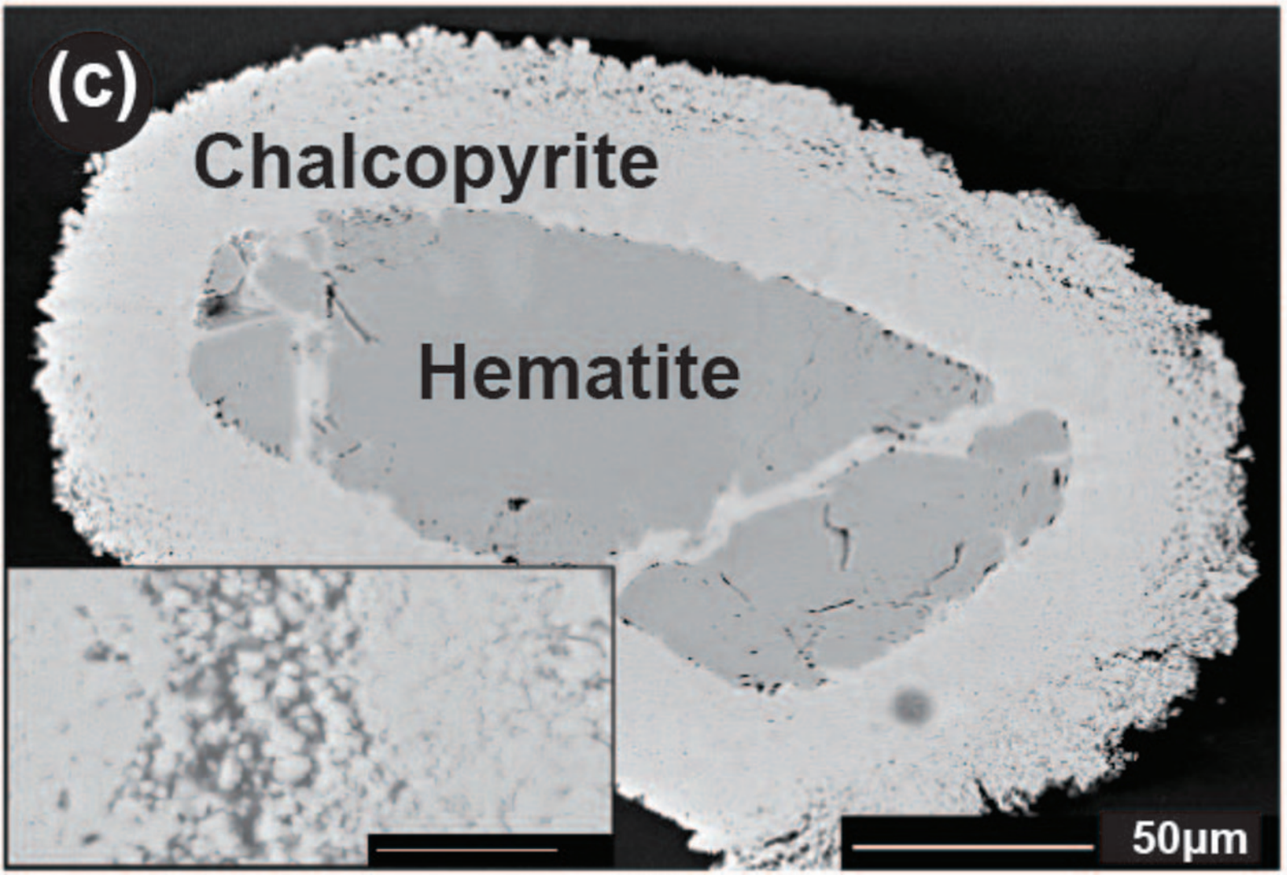
(c)
Chalcopyrite
Hematite
50μm

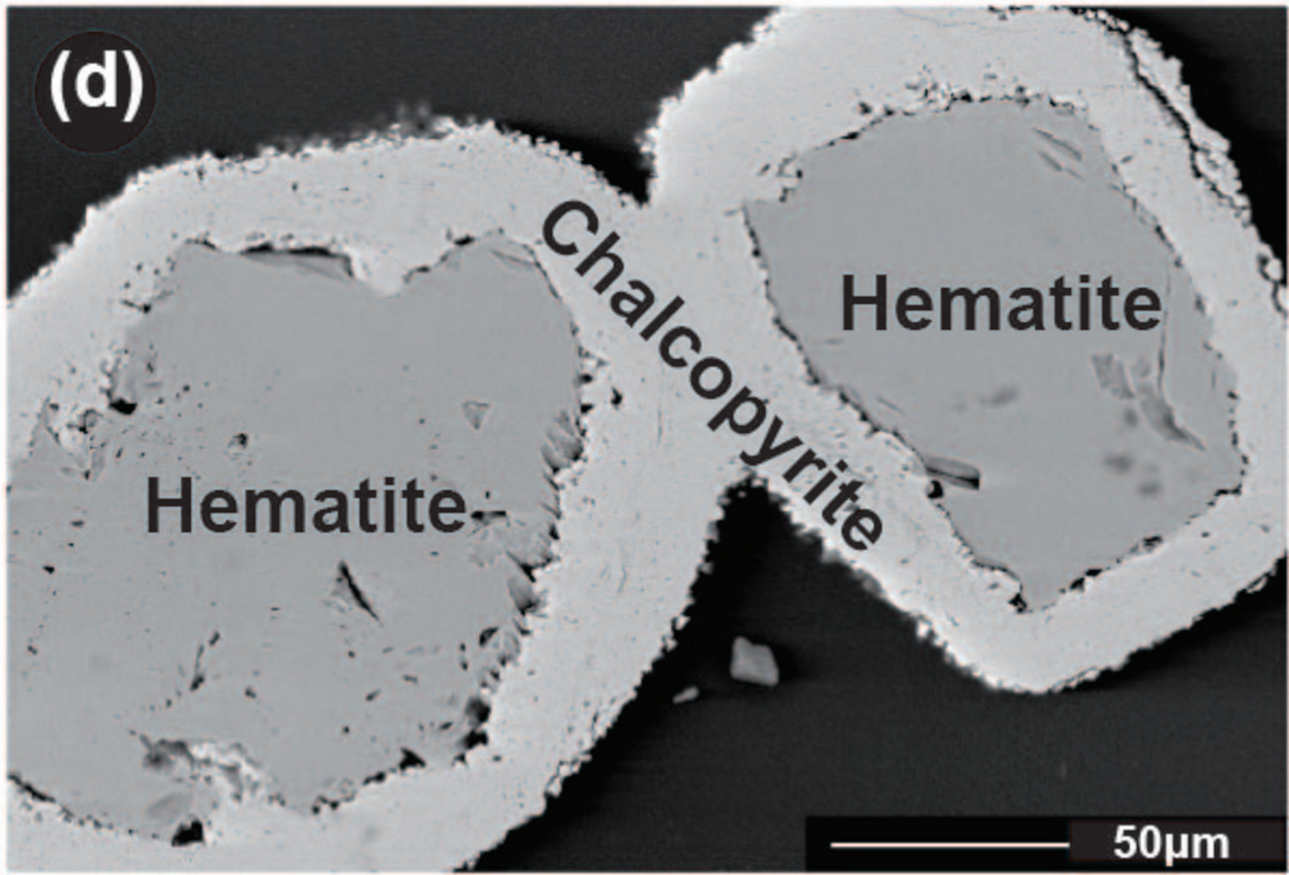
(d)
Hematite
Chalcopyrite
Hematite
50μm

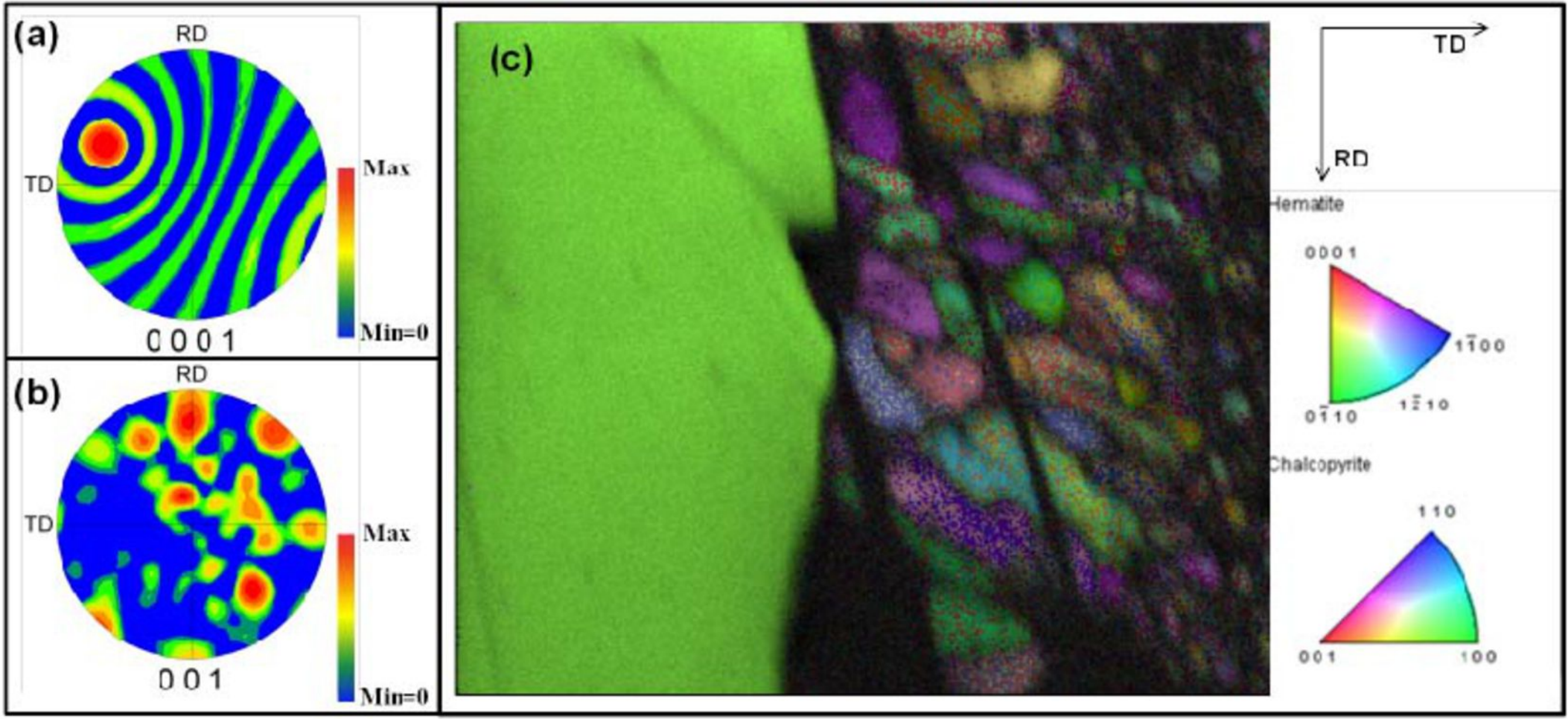
(a)
RD
TD
Max
Min=0
0 0 0 1
(b)
RD
TD
Max
Min=0
0 0 1
(c)
TD
RD
Hematite
0 0 0 1
1 1 $\bar{2}$ 0 0
0 $\bar{1}$ 1 0
1 $\bar{2}$ $\bar{1}$ 0
Chalcopyrite
1 1 0
0 0 1
1 0 0

(a)

50μm

(b)

20μm

(c)

Bornite

Hematite

Chalcopyrite

Bornite

50μm

(d)

Bornite

Chalcopyrite

Hematite

20μm

(e)

Bornite

Chalcopyrite

Hematite

20μm

(f)

50μm

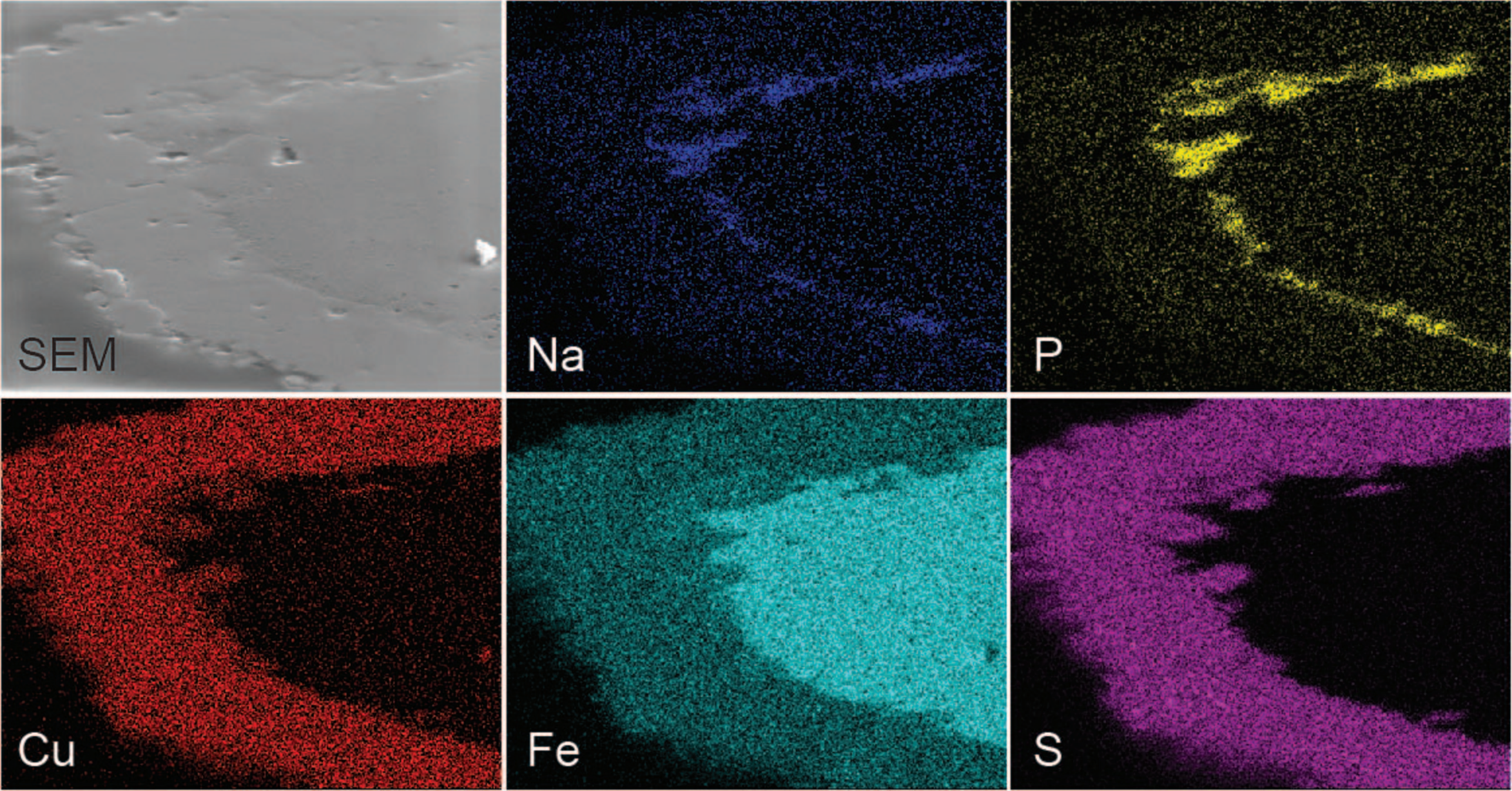
SEM
Na
P
Cu
Fe
S

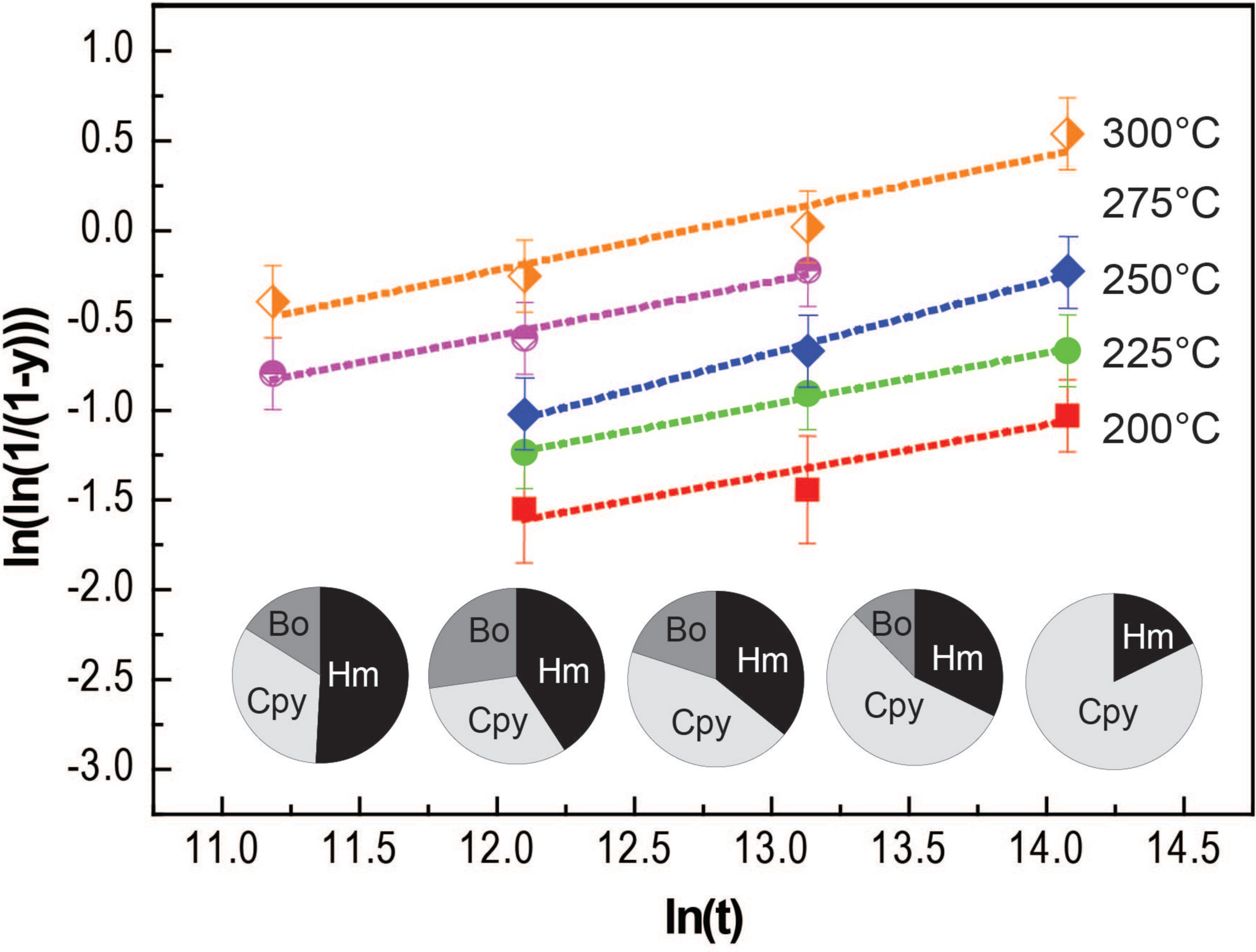
ln(ln(1/(1-y)))
1.0
0.5
0.0
-0.5
-1.0
-1.5
-2.0
-2.5
-3.0
11.0
11.5
12.0
12.5
13.0
13.5
14.0
14.5
ln(t)
300°C
275°C
250°C
225°C
200°C
Bo
Hm
Cpy
Bo
Hm
Cpy
Bo
Hm
Cpy
Bo
Hm
Cpy
Hm
Cpy

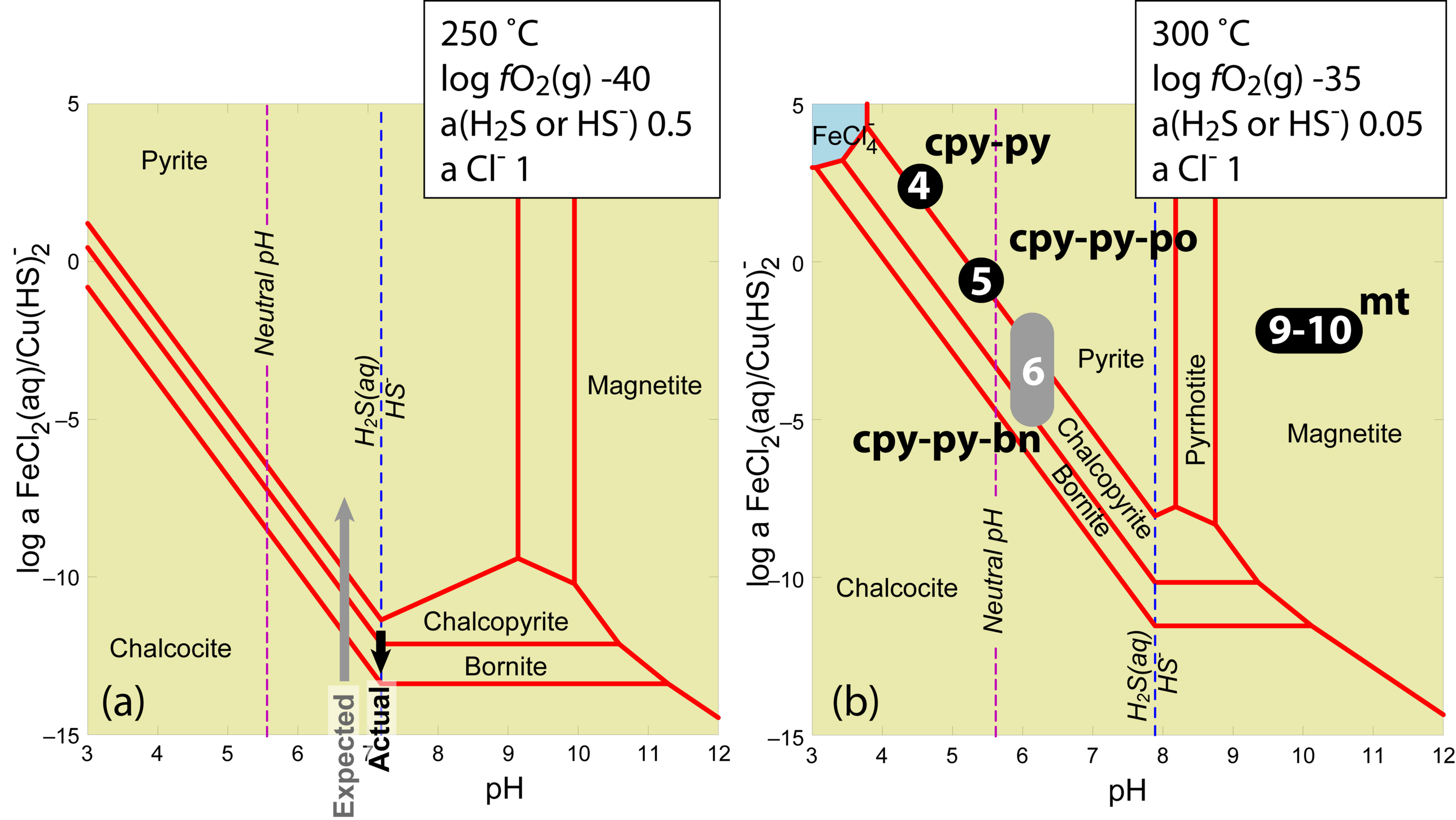
250 ˚C
log fO_2(g) -40
a(H_2S or HS^-) 0.5
a Cl^- 1
Pyrite
Neutral pH
H_2S(aq)
HS^-
Magnetite
Chalcopyrite
Bornite
Chalcocite
(a)
Expected
Actual
log a $FeCl_2$(aq)/$Cu(HS)_2^-$
pH
300 ˚C
log fO_2(g) -35
a(H_2S or HS^-) 0.05
a Cl^- 1
$FeCl_4^-$
cpy-py
4
cpy-py-po
5
6
9-10
mt
Pyrite
Pyrrhotite
Magnetite
cpy-py-bn
Chalcopyrite
Bornite
Chalcocite
Neutral pH
H_2S(aq)
HS^-
(b)
log a $FeCl_2$(aq)/$Cu(HS)_2^-$
pH